J Mater Sci (2010) 45:4454–4461
DOI 10.1007/s10853-010-4528-y

Microstructure analysis of samples sintered at different gravitational conditions

Kathy Lu · Randall M. German

Received: 23 January 2010 / Accepted: 13 April 2010 / Published online: 29 April 2010

Abstract Tungsten heavy alloy samples liquid phase sintered under normal gravity and microgravity conditions are examined in this study for microstructure, phase, grain orientation, and lattice misorientation comparison. The focus is on understanding gravitational effects on the microstructure evolution as a function of location in the samples sintered using different holding times. This analysis shows that gravity has sub-grain level effects. The main differences are observed at the grain boundaries and in the relative orientation of the touching grains. Microgravity sintering is conducive for solid grain rotation into low lattice misorientation angle arrangement and potentially coalescence.

Introduction

Previously, we conducted extensive studies on liquid phase sintering of tungsten heavy alloys under different gravitational conditions (normal gravity and microgravity on the Space Shuttle *Columbia* in 1997) [1–5]. At the time of those studies, the main focus was on gravitational effects with respect to microstructure homogeneity, grain growth, phase separation, and sample shape distortion. Presintering effects on liquid phase sintering densification during both ground gravity and microgravity sintering were reported to be significant. Presintering plays an important role in the quantity, mobility, and location of the pores in the sample. Solid–liquid separation is closely related to densification and shape distortion. In the ground-based sintering, the cold-isostatically pressed sample has the most uniform solid–liquid distribution with the largest shrinkage. In the microgravity sintering, the vacuum-presintered sample shows the largest degree of densification and elimination of pores. Coupled with the diffusion through the liquid phase, there are simultaneous solid-state sintering and grain growth by grain coalescence [1, 6]. The dihedral angle determines the solid-state contiguity and the grain growth rate. The liquid phase diffusion contribution to grain growth is at least one-order of magnitude higher than the solid-state diffusion contribution. As the alloy composition changes, the grain growth contributions from liquid phase diffusion, solid-state diffusion, and coalescence also change, which, in turn, causes grain size, grain size distribution, and contiguity variations.

While much work has been accomplished in the liquid phase sintering of tungsten heavy alloys under different gravitational conditions, a new technique has emerged for microstructure analysis in the past decade: electron backscatter diffraction pattern (EBSD) [7–11]. In EBSD, a diffraction pattern is created by focusing an electron beam on the surface of a specimen inclined with respect to the incident beam with a small angle (approximately 20°). Upon striking the sample, a shower of scattered electrons is generated from a small volume within the sample. The electrons are scattered in all directions. Some electrons escape by scattering with the atomic planes. The collection of these backscattered electrons with a phosphor screen in the microscope chamber produces a diffraction image. The bands in the pattern correspond to the crystallographic planes in the diffracting volume. The resulting diffraction

K. Lu (✉)
Department of Materials Science and Engineering, Virginia Polytechnic Institute and State University, 213 Holden Hall-M/C 0237, Blacksburg, VA 24061, USA
e-mail: klu@vt.edu

R. M. German
Mechanical Engineering, San Diego State University, San Diego, CA 92182-1326, USA

pattern (Kikuchi pattern) can be captured and interrogated in real time, and computer algorithms allow the orientation of each diffraction pattern to be obtained and stored, from which the microstructure of the sample can be constructed. When a representation of the orientation at each grid point is plotted, a crystallographic map of the microstructure can be obtained. This is mostly known as crystal orientation mapping. A grain boundary is revealed in a map by the change in orientation from grain to grain [7]. As the phase and the crystal orientation data at each point in the measurement array can be obtained separately, this technique is ideal for complicated microstructure analysis with nanometer scale resolution possible.

Electron backscatter diffraction pattern has been used in different studies. Examples include characterizing the grain boundary properties and energy distributions of yttria [12], resolving the slight tetragonality of L1(0)-ordered γ-TiAl [13], understanding the coarsening of secondary phases in a two-phase Zr–2.5 Nb [14], and investigating the microstructural evolution of nickel particles during the high-velocity impact in the cold spray process [15]. EBSD arises from a region of a sample within roughly 50 nm from the surface [16], and the sample-detector geometry requires a very flat surface finish. For this reason, samples for EBSD analysis must be very flat and free of polishing-induced surface damage or surface contamination.

This work re-visits the tungsten heavy alloy samples sintered in the identical furnace with the only variation being the gravitational environment. The intent is to examine the microstructure, phase, grain orientation, and lattice misorientation characteristics. The goal is to understand the gravitational effect on the microstructures from the same locations of the samples sintered for different times and from different locations of the same samples sintered for the same amount of time.

Experimental procedure

All the samples had 78 W–15.4 Ni–6.6 Fe (wt%) composition and the sample preparation was detailed elsewhere [3]. In brief, W, Ni, and Fe powders at the above ratio were mixed and cold-isostatically pressed and green machined into oversized right circular cylinders. The cylinders were pre-sintered at 1,400 °C for 1 h in hydrogen and final dry machined into cylindrical compacts. Each sample was inserted into individual alumina crucibles, heated and evacuated and electron beam welded into tantalum cartridges. The triple contained cartridges were heated to 1,500 °C for either 1 min or 600 min sintering in the same furnace under either ground-based condition or during space shuttle flight under microgravity condition. The heating rate was 18 °C/min. The cooling rate was 3 °C/min to a temperature of 1,400 °C, well below the matrix solidification temperature of 1,465 °C, and then furnace cooling to ambient temperature. Microgravity sintering experiments were performed as part of the three missions of the space shuttle Columbia: the Second International Microgravity Laboratory (STS-65, July, 1994), the first flight of the First Microgravity Science Laboratory (STS-83, April, 1997), and its reflight (STS-94, July, 1997). Parallel runs were conducted under identical conditions, except for the presence of gravity.

For the EBSD sample preparation, the sintered samples were polished first with 400 grit SiC for 20 min, then 600 grit SiC for 20 min, and then 1,200 grit SiC for 40 min. After these steps, the samples were polished with 5 μm Al_2O_3 suspension for 40 min, 3 μm Al_2O_3 suspension for 40 min, then 1 μm diamond paste for 30 min, and then 1 μm Al_2O_3 suspension for 40 min. Furthermore, the samples were polished with 0.05 μm SiO_2 sol for 40 min before being switched to vibratory polishing using the same 0.05 μm SiO_2 sol for 60–80 min. In-between all the polishing steps, the samples were ultrasonically cleaned for 30 min, especially when the Al_2O_3 suspension was used. After the final polishing step, ultrasonic cleaning was carried out for more than 120 min.

The EBSD characterization was carried out using a scanning electron microscope (FEI Helios 600 NanoLab, Hillsboro, OR). For all the EBSD analyses, a 60 μm × 60 μm sized area was used for each EBSD run. Five different runs were carried out at five randomly chosen areas for a given sample location. The acceleration voltage was 20 kV and the beam current was 1.4 nA for the microscope. For each of the samples analyzed, the binning was 4 × 4, the step size was 1 μm, and the magnification was 2000×. Each point of the scanned areas from the samples had a scan time of 0.377 s and 4325 points were collected for each 60 μm × 60 μm sized area.

Results and discussion

Microstructure and phase analysis

The microstructures of the 78 W–15.4 Ni–6.6 Fe (wt%) alloy samples after different sintering conditions are shown in Fig. 1. Both the sample top and the sample bottom locations are examined (although in microgravity this is arbitrary and only designates the crucible opening). The continuous matrix is the Ni–Fe–W liquid phase and the round-shaped phase is the tungsten solid phase. Consistent with prior observations [1, 3], there is substantial solid–liquid phase separation for the ground-sintered samples. The sample top locations contain almost complete liquid phase. For the microgravity-sintered samples, no

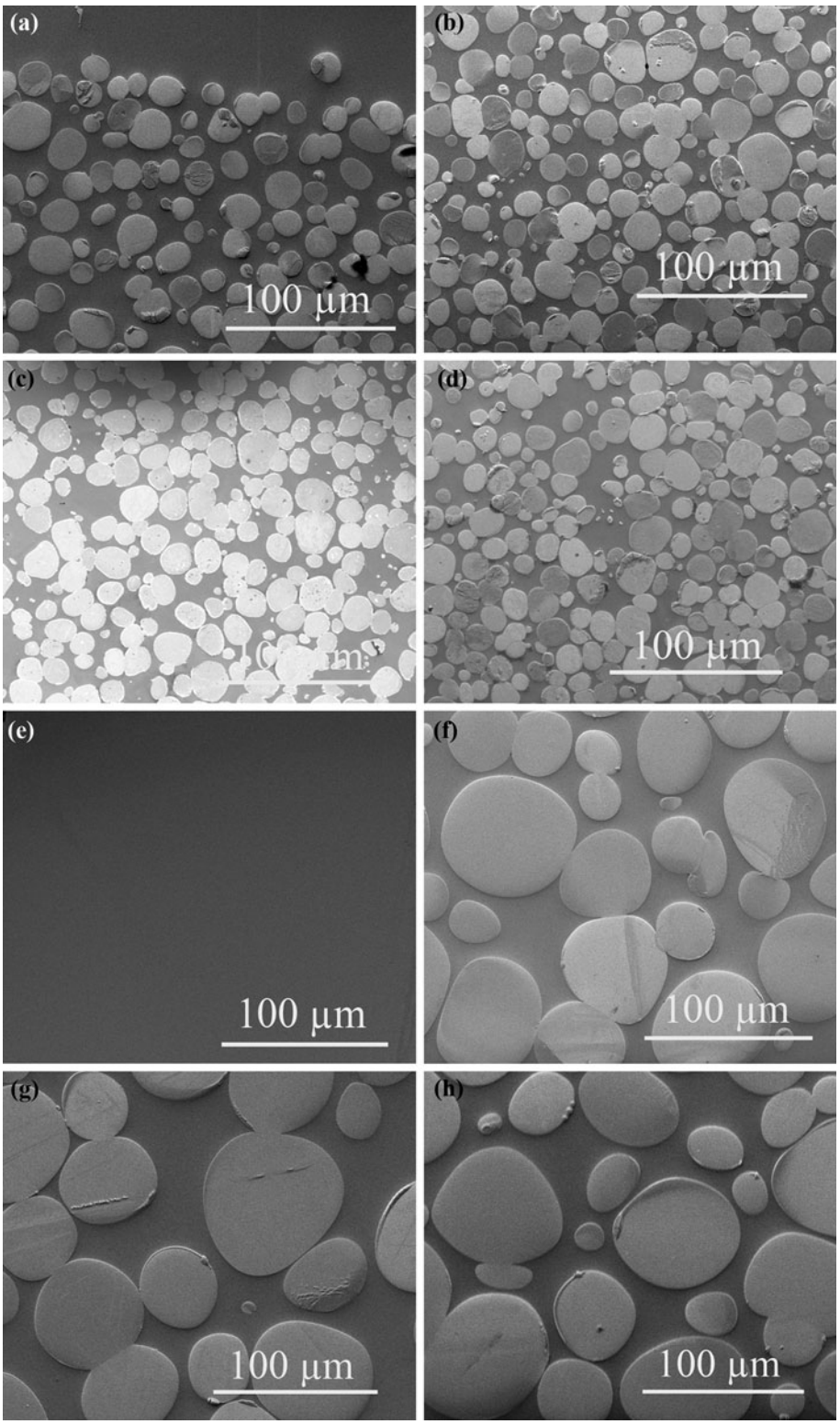

Fig. 1 78 W–15.4 Ni–6.6 Fe (wt%) alloy microstructures after sintering at 1,500 °C: **a** ground-based, 1 min, sample top, **b** ground-based, 1 min, sample bottom, **c** microgravity-based, 1 min, sample top, **d** microgravity-based, 1 min, sample bottom, **e** ground-based, 600 min, sample top, **f** ground-based, 600 min, sample bottom, **g** microgravity-based, 600 min, sample top, **h** microgravity-based, 600 min, sample bottom

solid–liquid phase separation is observed. In addition, substantial tungsten grain growth occurs after 600 min holding time at 1,500 °C for both the ground gravity and the microgravity sintering conditions (Figs. 1b vs. f and 1d vs. h). For the 1 min ground-sintered sample, there is a higher extent of grain–grain contacts at the sample bottom (Fig. 1b) than at the sample top (Fig. 1a), a natural consequence of tungsten grain settlement during sintering. For the 1 min microgravity-sintered sample, there is no clear grain–grain contact difference (Fig. 1c, d). After the samples are sintered

at 1,500 °C for 600 min, there are fewer tungsten grain–grain contacts for both sintering conditions. This is primarily because of the extensive grain growth and fewer grains in a given 60 μm × 60 μm area. For the ground gravity sintered sample, solid–liquid phase separation becomes more serious (Fig. 1e). No tungsten solid phase is observed at the similar top location to the 1 min ground gravity sintered sample (Fig. 1a). For the microgravity-sintered sample, there is no distinguishable solid–liquid phase separation (Fig. 1g, h). Because of the fewer grains in the view for the 600 min sintered samples at both ground gravity and microgravity conditions, no grain–grain contact difference is observed (Fig. 1f, h). However, a comparison of the microstructures for the same samples at low magnification shows more grain contacts and sintered grain boundaries for the ground gravity sintered sample (Fig. 2).

During the 78 W–15.4 Ni–6.6 Fe (wt%) alloy sintering, Ni and Fe melt and form the liquid phase when heated to 1,500 °C. Tungsten has ~26 wt% solubility in the Ni–Fe liquid phase at this sintering temperature [17, 18]. The liquid phase has 26 W–52 Ni–22 Fe (wt%) composition. Since tungsten has much higher density (19.3 g/cc) than nickel (8.9 g/cc) and Fe (7.9 g/cc), the atomic ratio of the liquid phase is 13 W–59 Ni–28 Fe. The liquid phase evolution process during cooling can be considered from Ni–Fe solid solution first. Considering the Ni:Fe weight ratio alone in the liquid phase (70 Ni:30 Fe), a solid solution forms after the samples are cooled below about 1,450 °C [19, 20]. The stable phase between 1,450 and 503 °C is the γ phase with faced centered cubic crystal structure. At temperatures below 503 °C, a series of phase transformation occurs and the stable phase from 200 °C to room temperature is the α phase. However, for the 26 W–52 Ni–22 Fe (wt%) system, the transformation of the γ phase into the α phase can take place quite sluggishly due to the slow diffusion of nickel and the hindrance of tungsten. In this work, the γ phase with faced centered cubic crystal structure is identified for the Ni–Fe–W liquid phase (simplified as Ni–Fe phase thereafter) after sintering as shown in Fig. 3 by the inverse pole figure and the Kikuchi pattern (taking the 1 min ground-sintered sample bottom location as an example). The higher temperature crystal structure of the liquid phase is retained. The Ni–Fe liquid phase region examined (60 μm × 60 μm size) is composed of primarily one crystallographic orientation with a few grid points oriented differently. As a result, the inverse pole figure shows mainly one crystallographic orientation for the entire liquid phase area examined. For the different

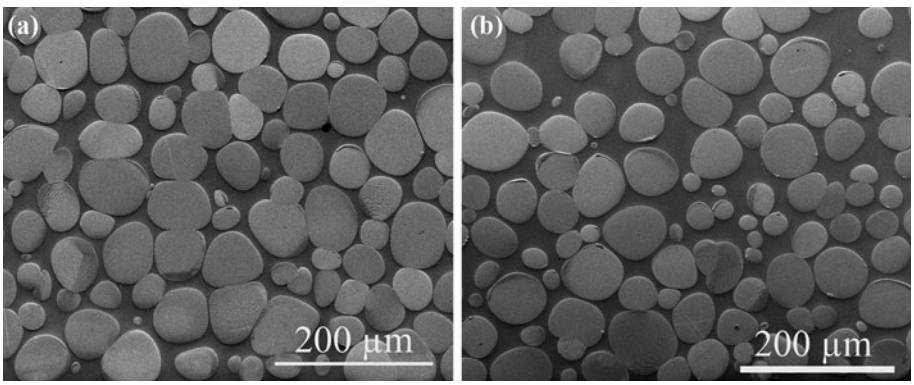

Fig. 2 Microstructures of 600 min sintered samples at low magnifications: **a** ground-based, 600 min, sample bottom, **b** microgravity-based, 600 min, sample bottom

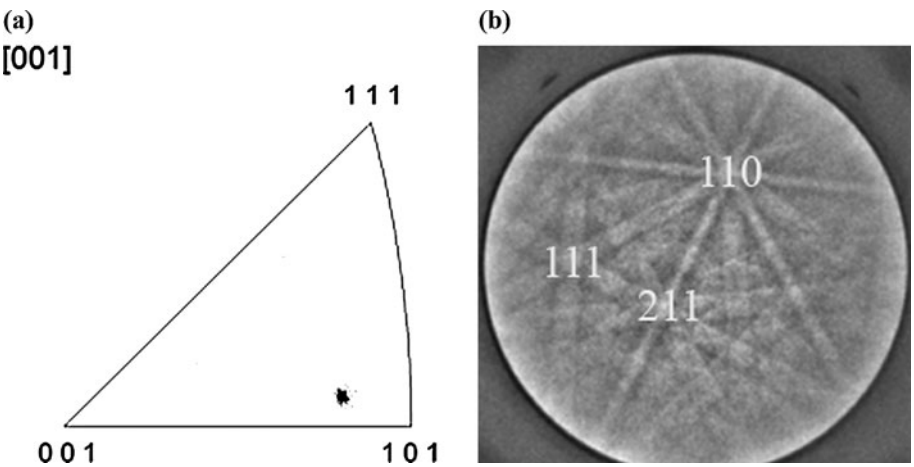

Fig. 3 **a** Ni–Fe phase inverse pole figure (taking 1 min ground-sintered sample bottom as an example). **b** Kikuchi pattern of the Ni–Fe phase showing the γ phase with face centered cubic crystal structure

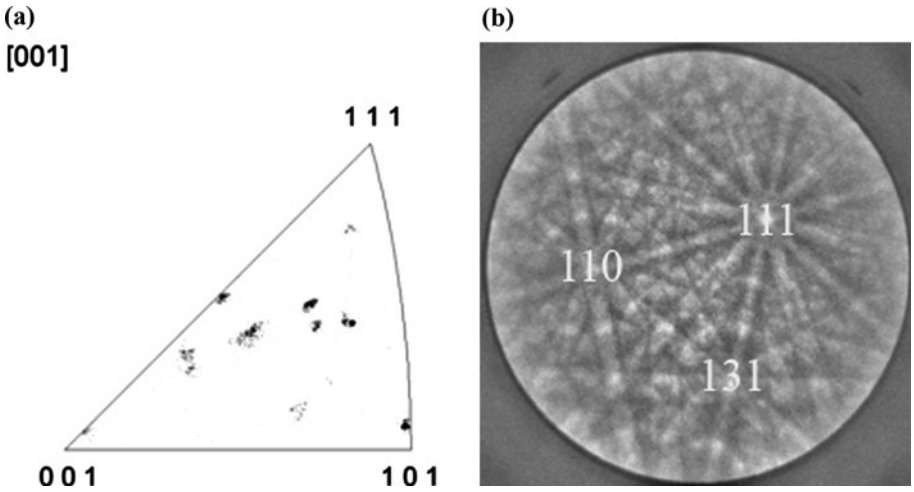

Fig. 4 **a** Tungsten phase inverse pole figure (taking 1 min microgravity-sintered sample bottom as an example). **b** Kikuchi pattern of the tungsten phase showing body centered cubic crystal structure

liquid phase regions of the same sample or different samples, the inverse pole figure shows that the crystallographic orientation changes gradually but generally one primary orientation is detected for an examined area.

Figure 4 shows the body centered cubic structure of the tungsten solid phase from both the inverse pole figure and the Kikuchi pattern (taking the 1 min microgravity-sintered sample bottom as an example). There is no tungsten crystal structure change during the sintering process. Since the area examined includes multiple tungsten grains, the inverse pole figure shows several crystallographic orientations with a random distribution. This means different tungsten grains are oriented differently and each tungsten grain has a very small range of crystallographic orientations after sintering. For the different locations of the same sample or different samples, the tungsten inverse pole figures show varying crystallographic orientations for different tungsten grains. However, no preferential tungsten grain orientation is observed for all the samples examined.

Crystal orientation mapping

For the samples that are ground or microgravity sintered for 1 min, the crystal orientation mapping results are shown in Fig. 5. Each color in the images represents a different crystallographic orientation. The continuous matrix phase is the Ni–Fe liquid phase and the round-shaped phase is the tungsten solid phase. The grains show elongated shapes because of the small sample tilting angle versus the incident beam used for the EBSD analysis. The images are not the conventional top view of the samples as shown in Fig. 1. Instead, the sample is slanted versus the viewing direction. As a result, the grains show elongated shapes when projected on a 2D image. The 600 min ground-sintered and microgravity-sintered samples show similar results but with fewer grains in the view because of the substantial grain growth. Because of this, the results for the 600 min sintered samples are not shown here. For the liquid phase, the crystal orientation mapping mostly shows one crystallographic orientation, demonstrated by the single color throughout an examined area. However, the crystallographic orientation of the liquid phase varies from sample to sample, shown by the liquid phase color changes for the four images. This result is consistent with the inverse pole figure and Kikuchi pattern changes observed for the Ni–Fe phase of the sintered samples. For the tungsten solid phase, each grain has a different crystallographic orientation but the bulk of individual grains is mostly (quasi-) single crystal with a very small crystallographic orientation variation range. This is supported by the different solid colors of individual tungsten grains while a few grains have slight color shade differences.

In some of the samples, the liquid phase shows some gradual and small crystallographic orientation changes in the same viewing area. This result is consistent with the inverse pole figure changes observed for the Ni–Fe phase of the sintered samples and means that the liquid phase generally crystallizes into one large, single crystal matrix. However, the presence of the solid tungsten grains and the cooling process itself can influence the crystallographic orientation to a certain extent. For the tungsten solid phase, again there are some gradual, minor crystal orientation variations in some grains but most grains show one orientation. Among the different tungsten grain sizes, the crystal orientation variations mainly occur in the large size grains. This means the solid tungsten grain atomic structure orientation evolves, even though slowly, with the tungsten grain growth.

From Fig. 5, it can also be observed that there is some crystal orientation changes at the liquid–solid phase boundaries, demonstrated by the color changes along the edges of the solid grains. This crystallographic orientation

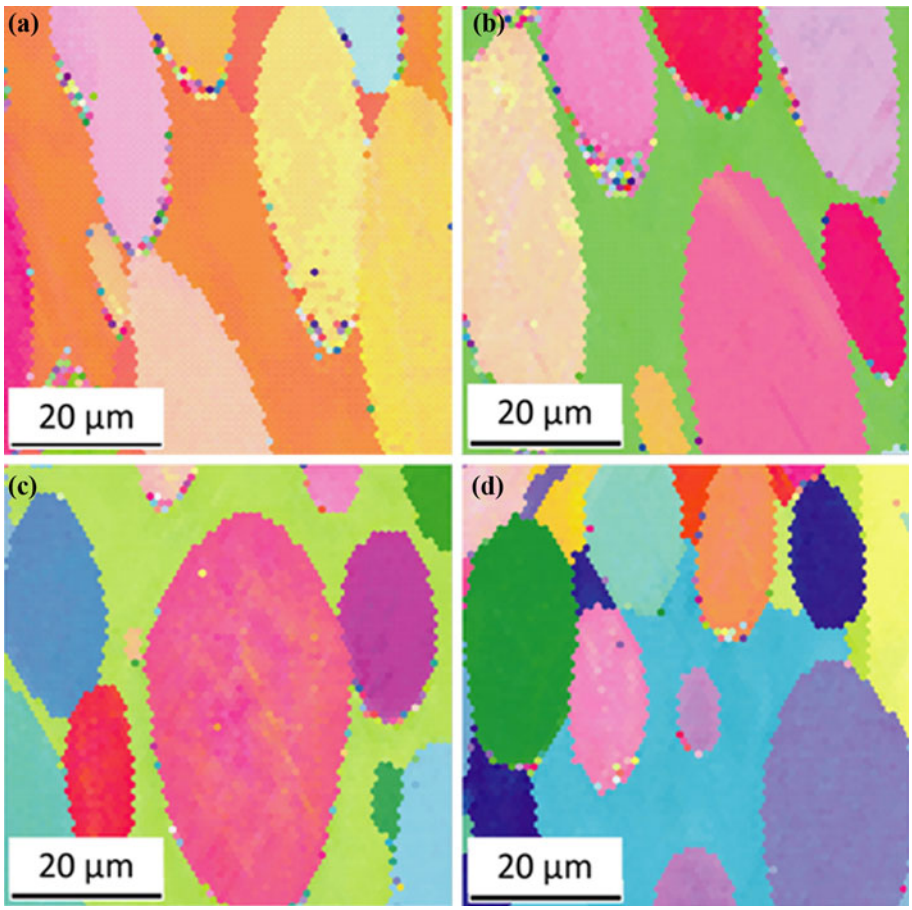

Fig. 5 Tungsten and Ni–Fe phase crystal orientation mapping for the samples that are ground and microgravity sintered for 1 min: **a** ground-based, sample top, **b** ground-based, sample bottom, **c** microgravity-based, sample top, **d** microgravity-based, sample bottom

change is believed to result from the variation of the tungsten re-precipitation from the liquid phase during cooling. The edges of the tungsten solid phase come from the dissolved tungsten species in the Ni–Fe liquid phase. Such drastic orientation changes mainly occur along the solid–liquid interfaces and the short, newly formed solid–solid grain boundaries. Since the temperature is lower during cooling (1,450–1,500 °C) and the time duration for the presence of the liquid is short, tungsten re-precipitates on the existing tungsten grain surfaces but in different crystal orientations in comparison to the grain bulk. The grain surface atomic structure evolves simultaneously with the additional tungsten grain growth. The edges of the solid tungsten grains are not fully integrated into the grains because of a lack of time and the slow-down of the diffusion process.

Lattice misorientation

From the EBSD results, grain boundaries inside each sintered sample can be mapped. Based on the grain boundary mapping, lattice misorientation at the grain boundaries can be analyzed. For the tungsten heavy alloy in this study, not all the tungsten grains are in contact with each other. Solid–liquid distribution difference under different gravitational conditions affects the amount of the touching grains. With this consideration, Fig. 6 shows the sample top and the sample bottom lattice misorientation results for the samples sintered for 1 min and 600 min at ground gravity and microgravity conditions. The misorientation angles examined are divided into three ranges: 2°–5°, 5°–15°, and 15°–180°.

Figure 6a shows the lattice misorientation angle data for the sample top locations. For the sample sintered at the ground gravity condition for 1 min, there is a very low amount of low angle (<15°) misorientation. For the sample sintered at the ground gravity condition for 600 min, there is an increased amount of 2°–5° angle misorientations at the sample top, while the high angle misorientation amount becomes lower. This phenomenon can be understood from grain contact point of view. At the beginning of the sintering, the grain–grain orientation is random from the forming process. During the ground gravity sintering the solid phase settles to the sample bottom. With the decreased content of the solid phase at the sample top, the rotation of the grains becomes less constrained. The lower

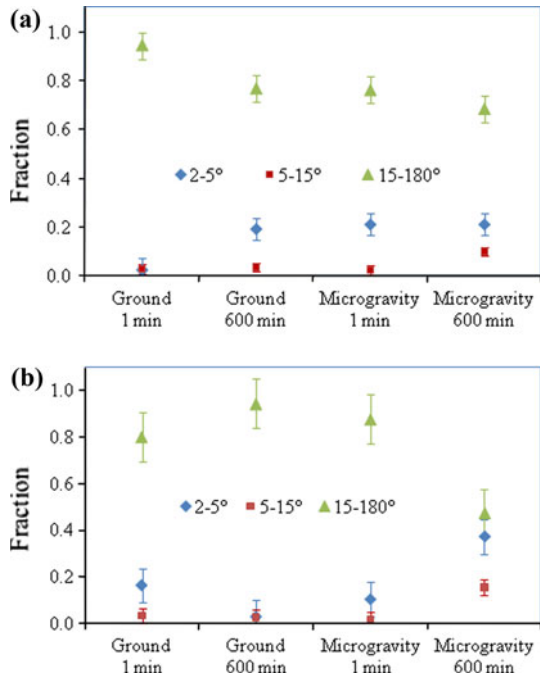

Fig. 6 Sample top and bottom lattice misorientation angle results for the samples sintered for 1 min and 600 min at ground gravity and microgravity conditions. **a** Sample top, **b** sample bottom

coordination number grains more easily rearrange to lower misorientation angles, leading to reduced system energy. For the sample sintered under the microgravity condition for 1 min, both the sample top and the sample bottom show a reasonable amount of low angle misorientation. This is because the tungsten grains are more uniformly distributed and the grains have more time to align in a low energy orientation before being sintered together (coalescence). With the sintering time increase to 600 min, both the sample top and the sample bottom show continued increase of low angle misorientation grain contacts. This is again because there is only very little solid–liquid separation (center-core versus top–bottom in the ground-based sintering) during microgravity sintering. The grain coordination number is more uniform throughout the sample and the grains are less constrained from rotation. Some contacting grains might also be able to adjust the relative orientation during sintering through diffusion to attain low misorientation angles. However, the misorientation change through the grain rotation before sintered bond formation is a much more efficient process than that through the diffusion process.

Figure 6b shows the lattice misorientation angle data for the sample bottom locations. For the sample ground sintered for 1 min, there is a slightly larger amount of 2°–5° misorientation angles. For the 600 min ground-sintered sample, the amount of the low misorientation angles decreases but statistically insignificant. Since the tungsten grains have a high coordination number at the sample bottom and the grain rotation is limited, this means the diffusion-induced low misorientation angle amount is not as important even after 600 min of sintering time. For the 1 min microgravity-sintered sample, there is no significant difference in lattice misorientation angle contacts. Again, the 600 min microgravity-sintered sample shows a larger amount of low angle lattice misorientations, consistent with the same sample top locations. From Fig. 6, it can be determined that both more dispersed tungsten grain distribution and longer sintering time are needed for the formation of low lattice misorientation angle contacts.

An additional comment to make is the potential relationship between the evolution of the low angle lattice misorientations and coalescence. Under the ground gravity sintering condition, there is an insignificant change in low angle lattice misorientations. Under the microgravity sintering condition, however, the amount of low angle lattice misorientations increases, which is expected since grains can rotate without much restriction. On the other aspect, coalescence should be more preferable in low angle misorientations and the fraction of low angle boundaries gives a view of that. For the current study, this means the microgravity sintering condition should be more conducive for coalescence. Even though it is often speculated that 5% of grains coalesce during sintering, the estimate can be as high as 22%. Long time sintering might remove some low angle misorientations for the grains that are fully sintered together through coalescence. However, at the same time more new contacts might form. As a result, the microgravity-sintered samples still have more low angle lattice misorientations.

Conclusions

Tungsten heavy alloy samples sintered at both ground gravity and microgravity conditions are examined for microstructure, phase, grain orientation mapping, and grain boundary lattice misorientation. Grain level microstructure analysis shows the same solid–liquid separation and grain growth phenomena as reported earlier. Individual liquid and solid phases are mostly single crystals except for the grain surfaces, where tungsten re-precipitation during cooling due to solubility changes creates different crystallographic orientations. Gravity-induced solid phase settlement affects the touching tungsten grain orientations while microgravity sintering is beneficial for uniform solid distribution and lower grain coordination number, which allow grains to rotate and form low misorientation angles. This, in turn, can be conducive for grain coalescence. The EBSD analysis provides a robust method to identify crystalline phases and the relative orientation of grains.

Acknowledgements The authors are grateful of Manoj Mahapatra for polishing the samples for the EBSD work and John McIntosh for assistance during the EBSD data collection.

References

1. Lu K, German RM (2000) J Mater Sci 36:3385. doi:10.1023/A:1017943524875
2. Marx BM, Lu K, German RM (2001) Int J Powder Metall 37:11
3. Lu K, German RM, Iacocca RG (2001) Metall Mater Trans A 32A:2097
4. Johnson JL, Upadhyaya A, German RM (1998) Metall Mater Trans B 29B:857
5. Tewari A, Gokhale AM, German RM (1999) Acta Mater 47:3721
6. Johnson JL, Campbell LG, Park SJ, German RM (2009) Metall Mater Trans A 40:426
7. Schwartz AJ, Kumar M, Adams BL (2000) Electron backscatter diffraction in materials science. Kluwer Academic, New York, NY
8. Randle V (2004) Int Mater Rev 49:1
9. Baba-Kishi KZ (2002) J Mater Sci 37:1715. doi:10.1023/A:1014964916670
10. Humphreys FJ (2001) J Mater Sci 36:3833. doi:10.1023/A:1017973432592
11. Dingley DJ, Randle V (1992) J Mater Sci 27:4545. doi:10.1007/BF01165988
12. Dillon SJ, Rohrer GS (2009) J Am Ceram Soc 92:1580
13. Zambaldi C, Zaefferer S, Wright SI (2000) J Appl Crystallogr 42:1092
14. Hiwarkar VD, Sahoo SK, Krishna KVM, Samajdar I, Dey GK, Srivastav D, Tewari R, Banarjee S, Doherty RD (2009) Acta Mater 57:5812
15. Zou Y, Qin W, Irissou E, Legoux JG, Yue S, Szpunar JA (2009) Scr Mater 61:899
16. Nowell MM, Witt RA, True B (2005) Microsc Microanal 11:2005
17. German RM (1995) Metall Mater Trans A 26:279
18. Guillermet AF, Ostlund L (1986) Metall Trans A 17:1809
19. Brandes EA, Brook GB (1992) Smithells metals reference book. Butterworth-Heinemann, Boston, MA
20. Massalski TB, Murray JL, Bennett LH, Baker H, Kacprzak L (1986) Binary alloy phase diagrams. American Society for Metals, Metals Park, OH